

Time-resolved correlative optical microscopy of charge-carrier transport, recombination, and space-charge fields in CdTe heterostructures

Darius Kuciauskas,^{1,a)} Thomas H. Myers,² Teresa M. Barnes,¹ Søren A. Jensen,¹ and Alyssa M. Allende Motz³

¹National Renewable Energy Laboratory, 15013 Denver West Parkway, Golden, Colorado 80401, USA

²Texas Materials Science, Engineering, and Commercialization Program, Texas State University, 601 University Drive, San Marcos, Texas 78666, USA

³Department of Physics, Colorado School of Mines, Golden, Colorado 80401, USA

(Received 1 December 2016; accepted 2 February 2017; published online 23 February 2017)

From time- and spatially resolved optical measurements, we show that extended defects can have a large effect on the charge-carrier recombination in II–VI semiconductors. In CdTe double heterostructures grown by molecular beam epitaxy on the InSb (100)-orientation substrates, we characterized the extended defects and found that near stacking faults the space-charge field extends by 2–5 μm . Charge carriers drift (with the space-charge field strength of 730–1,360 V cm^{-1}) and diffuse (with the mobility of $260 \pm 30 \text{ cm}^2 \text{ V}^{-1} \text{ s}^{-1}$) toward the extended defects, where the minority-carrier lifetime is reduced from 560 ns to 0.25 ns. Therefore, the extended defects are nonradiative recombination sinks that affect areas significantly larger than the typical crystalline grains in II–VI solar cells. From the correlative time-resolved photoluminescence and second-harmonic generation microscopy data, we developed a band-diagram model that can be used to analyze the impact of extended defects on solar cells and other electronic devices. *Published by AIP Publishing.*

[<http://dx.doi.org/10.1063/1.4976696>]

To investigate the fundamental performance limits of II–VI solar cells, single crystals and epitaxial heterostructures have recently been used in solar cells that reached an open-circuit voltage of $>1 \text{ V}$.^{1,2} Epitaxial materials are also used in other optoelectronic devices, such as sensors and detectors. All applications require an understanding of defects and their impact on electronic properties such as charge-carrier transport and recombination. Photoluminescence (PL) microscopy and imaging were applied to study the transport in III–V^{3–6} and II–VI heterostructures^{7–9} and in polycrystalline thin films.¹⁰ We extended this approach by using correlative second-harmonic generation (SHG) measurements. Interaction between the incident light wave and a DC electric field in the material generate EFISH (electric-field-induced second-harmonic) signals, and the optical EFISH measurements allow the analysis of the space-charge fields (SCFs) near the extended defects.

We report the electronic properties of CdTe heterostructures grown by molecular beam epitaxy (MBE) on InSb (100) substrates. Polar (100) surfaces have high surface energy and can nucleate the extended defects, such as twins and stacking faults.¹¹ We found that in the high-quality epitaxial heterostructures, **a single extended defect can affect carrier recombination in an area larger than $100 \mu\text{m}^2$** . We also found that drift due to the SCF can increase the impact of recombination.

Double heterostructures (DHs) were grown by MBE and characterized as described in Zaunbrecher *et al.*¹² Confocal PL (c-PL) was used to identify the extended defects and to determine their density.¹² The incorporation of 0.8% Se in the CdTe absorber and the buffer provided better lattice

matching to InSb and allowed the growth of thicker absorbers without strain relaxation. For the DH studied here, the CdTe epilayer thickness was 5 μm , the extended defect density estimated from c-PL was $\approx 10^4 \text{ cm}^{-2}$, and the minority-carrier lifetime was 560 ns. Passivation with 30-nm-thick epitaxial $\text{Mg}_x\text{Cd}_{1-x}\text{Te}$ ($x=0.25\text{--}30$) reduced the interface recombination velocity to 160 cm s^{-1} .¹² The DHs were not intentionally doped; the background doping was p-type at $\approx 3 \times 10^{14} \text{ cm}^{-3}$.

The nonlinear optical microscopy employed here uses the local generation/local signal collection geometry (Figure 1(a)). Such measurements have two-times-higher spatial resolution than microscopy in the local generation/global collection configuration.⁶ We used 1030 nm excitation with 300-fs pulses at 1.1 MHz repetition rate. For the PL/time-resolved PL (TRPL) measurements on semiconductors with a bandgap of 1.5 eV, this wavelength allows two-photon excitation (2PE).¹³ The excitation energy was 0.05–0.20 pJ pulse⁻¹, and the excitation beam was focused with a Zeiss A-Plan 40 \times NA0.65 objective.¹⁴ As shown below, such excitation corresponds to low-injection conditions. Photon counting detectors (PDM from Micro Photon Devices) with 10-nm bandpass interference filters were used in PL (840 nm) and SHG (515 nm) measurements. Time-correlated single-photon counting (TCSPC) with a PHR800 router and PicoHarp 300 (Picoquant) afforded $\approx 90 \text{ ps}$ time resolution that was mostly limited by the time response of the single-photon detectors. The sample was translated with mechanical xyz stages, and at each coordinate the TRPL/SHG data were integrated for 0.1–1 s. Because deconvolution was not used in data analysis, the PL and SHG data were time-integrated in 0.1-ns steps. Overall, the microscope provides an estimated 0.5- μm lateral (x and y) and 0.1-ns temporal

^{a)}Author to whom correspondence should be addressed. Electronic mail: darius.kuciauskas@nrel.gov

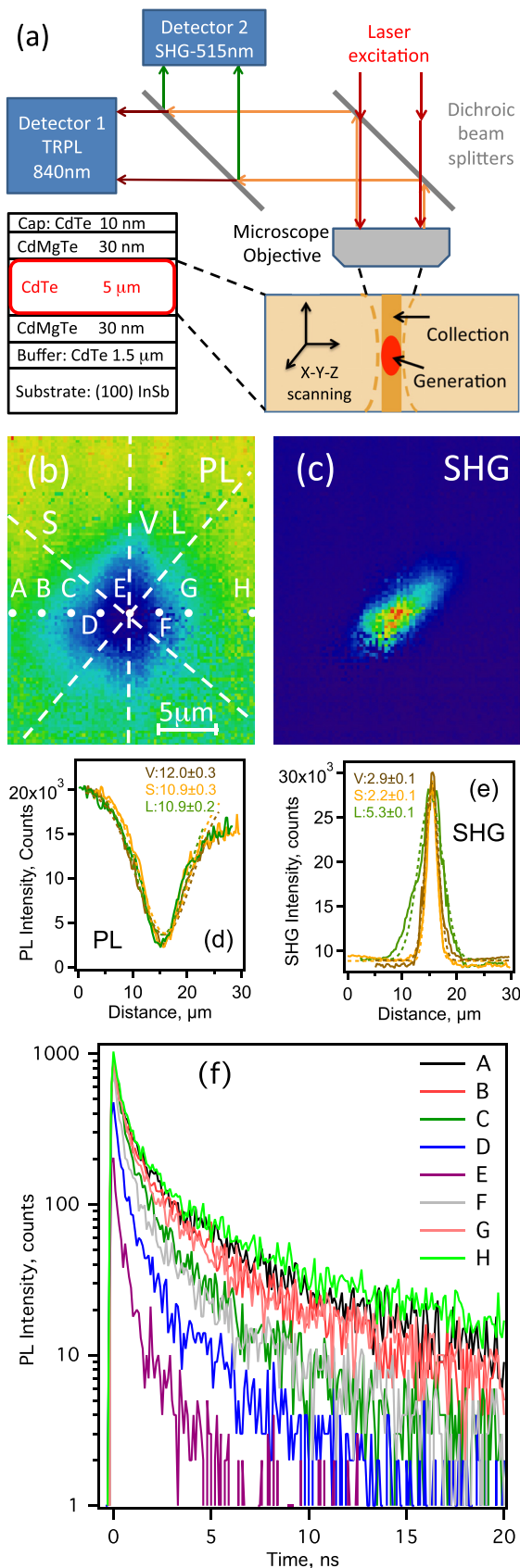


FIG. 1. (a) Experimental setup and DH sample structure. (b) and (c): Integrated PL and SHG images for the same area. Letters (A–H) indicate pixel locations for which TRPL decays are shown in (f). Dashed lines V, L, and S in (b) mark directions where charge-carrier transport was analyzed in Figure 3 and where linear intensity profiles are shown for PL (d) and SHG (e). Dashed lines in (d) and (e) show the Gaussian fits to the data, and legends indicate the full-width-at-half-maximum values for the Gaussian fits.

resolution for the PL and SHG measurements. The axial (z) resolution for 2PE PL microscopy in a semiconductor with a refractive index $n = 2.85$ is $\approx 3 \mu\text{m}$.^{14,15} The axial resolution for SHG microscopy is $\approx 0.5 \mu\text{m}$ because the SHG signal at 515 nm is strongly reabsorbed in CdTe.

To characterize the influence of the extended defects on the electronic characteristics of II–VI heterostructures, Figure 1 shows PL (b) and SHG (c) images near one extended defect. The images were obtained by time-integrating the PL and SHG data measured in an area $20 \times 25 \mu\text{m}^2$ with a pixel size of $0.25 \mu\text{m}$. Several TRPL decays at individual pixels are shown in (f). At the center of the extended defect (pixel E), the PL decay can be fit with a 0.25 ns lifetime. This **short lifetime indicates fast nonradiative recombination due to the Shockley-Read-Hall (SRH) recombination centers associated with the extended defect**. When the distance to the center of the image increases, the decays have longer lifetimes and non-exponential shapes. For example, the decays at pixels A and H (same distance to the center) are nearly identical. We have previously shown that when the carrier diffusion length is $>1 \mu\text{m}$, 2PE TRPL microscopy data in the local excitation/local collection geometry indicate not only recombination but also charge-carrier transport.¹⁶ These characteristics were also analyzed with numerical simulations¹⁷ and analytical modeling.¹⁸ Therefore, the decays in Figure 1(f) are dominated by charge-carrier transport. Unlike the case analyzed earlier,^{16–18} transport near the extended defect is not isotropic due to the recombination sink (extended defect). Therefore, we apply time-resolved microscopic analysis.

Figure 1(c) shows an SHG image measured simultaneously with the PL data. The weaker SHG background is present everywhere in the image, but SHG is approximately three times stronger near the extended defect (see the SHG intensity profiles in Figure 1(e)). This enhancement is attributed to the EFISH mechanism, where the second harmonic of the incident light is generated due to the SCF near the extended defect in the heterostructure. EFISH microscopy has been applied to organic bulk heterojunctions,¹⁹ organic transistors,²⁰ and metal-silicon junctions.²¹ Our data show that EFISH microscopy could be applied for the SCF analysis near the extended defects. Because the SCF affects the carrier dynamics, the field strength can be estimated from the TRPL data (see Figure 3). This is an important advantage of correlative microscopy, where the SHG/EFISH data indicate the spatial distribution of the SCF, and analysis of the carrier dynamics provides the strength of the SCF.

In contrast, when similar measurements were applied near the threading-dislocation extended defects in DHs grown on (211)B-orientation CdTe substrates, the second-harmonic enhancement was not observed.⁹ Comparison suggests that space-charge fields are absent (or are weaker) near threading dislocations. Transport near dislocations in the GaAs/GaInP DH could also be described by the diffusion model.^{4–6}

When Gaussian fits are used to describe the intensity profiles in PL (Figure 1(d)) and SHG (Figure 1(e)) images, the full width at half maximum (FWHM) is larger for the PL data (e.g., in the S direction, $\text{FWHM}_{\text{PL}} = 10.9 \mu\text{m}$ and $\text{FWHM}_{\text{SHG}} = 2.2 \mu\text{m}$). Because the reduced PL intensity at the center is attributed to recombination, the data indicate

that carriers can reach nonradiative recombination sites over a distance of $>10\ \mu\text{m}$. Such data suggest transport to the SRH recombination centers.^{3–7,9,12} Drift and diffusion processes in the dynamics could be resolved from the time-resolved microscopy data described below.

The time-dependent PL and SHG images in Figure 2(a) were obtained by normalizing the intensity in each frame. The size of the dark area in the PL images (corresponding to low PL intensity) is increasing over time. Because the charge-carrier lifetime at the center is very short (0.25 ns) due to the fast nonradiative recombination, carriers generated in other areas can diffuse (and drift; see below) toward the extended defect and nonradiatively recombine there. As shown in Figure 2(b), the Gaussian fits to PL intensity profiles were used to numerically evaluate the time-dependent FWHM for the region affected by recombination. For this orientation (vertical line in the middle of the frame), the FWHM increases from $5.2 \pm 0.7\ \mu\text{m}$ at 0.1 ns to $9.2 \pm 0.2\ \mu\text{m}$ at 1.9 ns ($1.8 \times$ increase) and $16.9 \pm 1.2\ \mu\text{m}$ at 20.9 ns (additional $1.8 \times$ increase). At $>20\ \text{ns}$, almost all of the $20 \times 25\ \mu\text{m}^2$ region is affected by recombination due to the extended defect.

In contrast to the PL data, the size of the bright feature in the SHG images in Figure 2 does not increase (FWHM = $2.9 \pm 0.1\ \mu\text{m}$ at 0.1 ns and $3.0 \pm 0.1\ \mu\text{m}$ at 1 ns), and the SHG time dependence is limited by the temporal response of the detector. Therefore, SHG/EFISH probes the interaction between the space-charge field in the material and the optical field,^{19–21} whereas PL probes carrier dynamics.^{3,7,9}

To describe the charge-carrier transport characteristics, in Figure 3 we analyze the time-dependent FWHM for the region where the PL intensity is reduced due to nonradiative recombination. At 0–2 ns, the size of the defect feature increases more rapidly and then continues to expand more slowly. The second phase of the increase is linear on the (FWHM)² vs. time scale and independent of the direction in the epilayer plane. By fitting these data to the two-dimensional diffusive transport model, we determine the charge-carrier diffusion coefficient D by using^{3,7}

$$(FWHM)^2 = 16\ln(2)Dt + 4\ln(2)(FWHM_0)^2, \quad (1)$$

where t is time and $FWHM_0$ is the initial FWHM for the carrier distribution. The fits in Figure 3(a) yield $D = 6.7 \pm 0.3\ \text{cm}^2\ \text{s}^{-1}$ (V direction), $D = 6.1 \pm 0.2\ \text{cm}^2\ \text{s}^{-1}$ (S direction), and $D = 7.7 \pm 0.2\ \text{cm}^2\ \text{s}^{-1}$ (L direction). The averaged charge-carrier mobility calculated using Einstein's relationship is $\mu = 260 \pm 30\ \text{cm}^2\ \text{V}^{-1}\ \text{s}^{-1}$. Figure 3(b) shows that when the excitation power is reduced 4 times (due to 2PE, injection is reduced 16 times), the time dependence for the FWHM is essentially unchanged. An intensity-independent carrier mobility indicates that the analysis is for electrons (minority carriers). Low injection is also suggested from the two-photon absorption coefficient ($\beta \approx 25\text{--}30\ \text{cm}\ \text{GW}^{-1}$ at 1000–1400 nm)²² and the excitation peak power ($I \approx 0.8\ \text{GW}\ \text{cm}^{-2}$). The product $\beta \times I \approx 20\ \text{cm}^{-1}$ is equivalent to the linear absorption coefficient. Because the excitation photon flux is $1.3 \times 10^{15}\ \text{photons}\ \text{cm}^{-2}$ and the absorption coefficient is small, injection is estimated to be lower than the background doping.

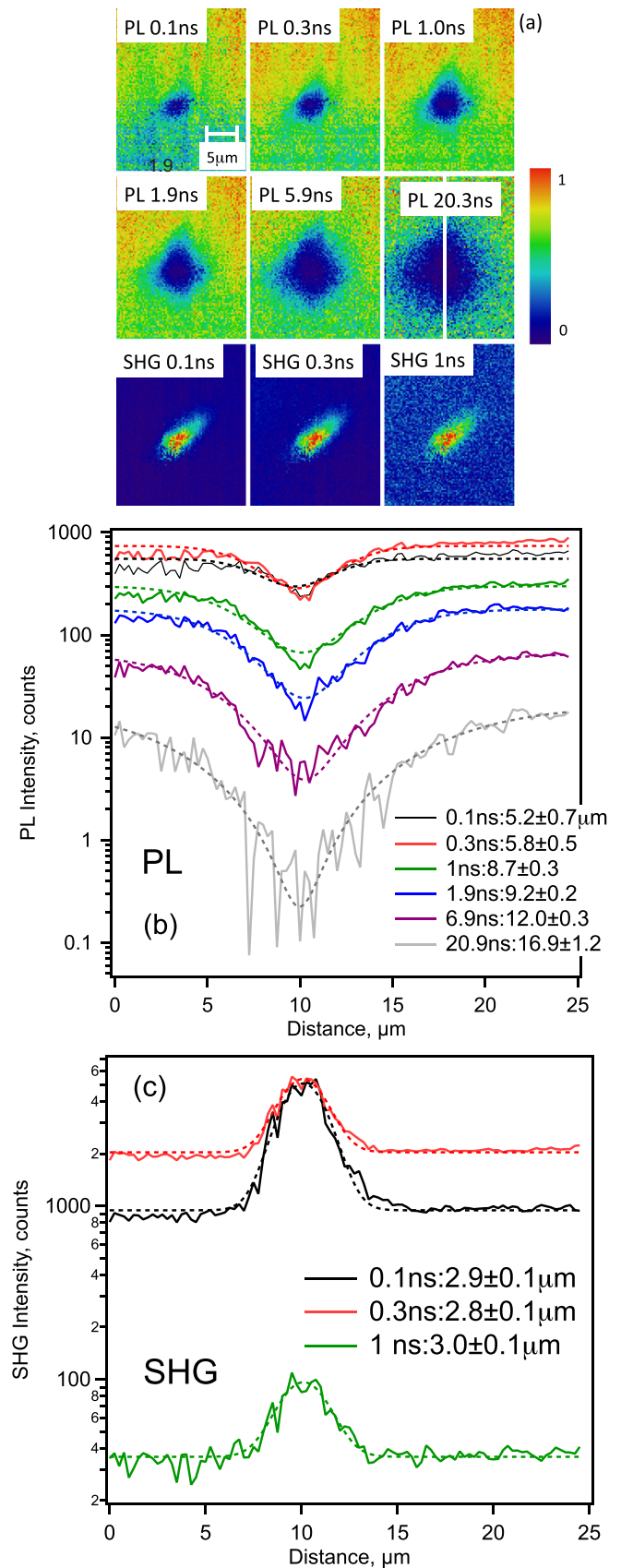


FIG. 2. (a) Time-resolved PL and SHG images at times indicated in the insets. The data in each image are normalized to illustrate the time-dependent increase in the area affected by recombination. Vertical line in the frame “PL 20.3 ns” indicates the location for which several time-dependent linear intensity profiles are shown for PL (b) and SHG (c). Gaussian fits in (b) and (c) are shown as dashed lines, and FWHMs are given in the legends.

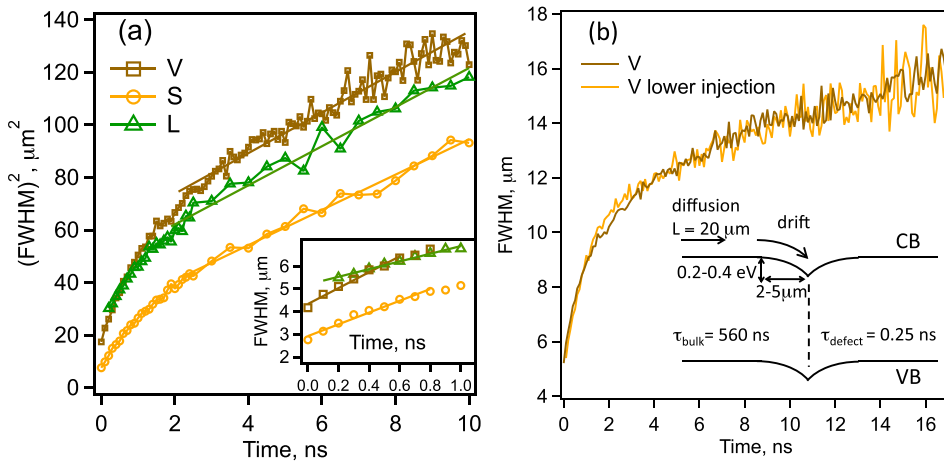


FIG. 3. (a) Time-dependent $(FWHM)^2$ and FWHM (inset) for the three directions indicated in Figure 1(b). (b) Comparison of FWHM data when injection differs by $16\times$. Inset in (b) shows band diagram that summarizes the results of this study.

The initial growth phase in the FWHM data in Figure 3 can be related to drift in the SCF. If the extended defects have positive charge, the minority carriers (electrons) will drift toward this area and recombination will affect a larger area than it would in the absence of SCF. For example, in the V direction, the size of the recombination region approximately doubles in size due to drift (see Figure 3(b)).

The inset in Figure 3(a) shows that the drift velocity (estimated as slope of FWHM vs. time) is the highest in the V direction. We estimate the SCF strength E_{SCF} from

$$E_{SCF} = \frac{1}{\mu} \frac{\Delta(FWHM)}{\Delta t}. \quad (2)$$

If we assume that drift and diffusion mobilities are the same, the fits indicate $E_{SCF,V} = 1360 \pm 80$ V cm^{-1} , $E_{SCF,L} = 730 \pm 35$ V cm^{-1} , and $E_{SCF,S} = 820 \pm 47$ V cm^{-1} .

The SCF near the extended defects could be created by charged impurities, strain,²³ or charge separation. The charge separation at pairs of partial dislocations was predicted from first-principles calculations.²⁴ Stacking faults are usually bordered by partial dislocations, and such dislocations could be recombination centers.^{25,26} The charge-carrier lifetimes could be reduced due to recombination at dislocations in II–VI heterostructures.^{7,8} Calculated band-bending due to the charge separation²⁴ is similar to our experimental results, and we also observe fast nonradiative recombination at the extended defects. It was suggested that the extended defects in CdTe could include wurtzite layers formed by closely spaced lamellar twins.²⁷ According to the calculated band alignment at the zinc-blende/wurtzite interface,²⁷ the wurtzite region would repel electrons, but we found that the SCF leads to electron drift toward the extended defects. Therefore, our data are in agreement with the model of recombination at partial dislocations/stacking faults, but not with the model of recombination due to the defects at the zinc-blende/wurtzite interface.

Data from our study can be summarized in the band diagram shown in the inset of Figure 3(b). The charge-carrier lifetime in the DH ($\tau_B = 560$ ns) is limited by the SRH recombination due to point defects in the bulk and at the interfaces.¹² The lifetime near the extended defects is reduced to 0.25 ns; therefore, the extended defects are

recombination sinks. The carrier diffusion length $L = \sqrt{D\tau_B} = 20 \mu m$, and the extent of recombination due to a single defect is consistent with this estimate. The microscopic SHG/EFISH images indicate the spatial distribution of the space-charge field. Depending on the orientation in the epilayer plane, the SCF can be described by the $FWHM = 2-5 \mu m$. The free carriers in the DH would screen the fixed charges. The screening length (depletion width) with the background doping of $3 \times 10^{14} cm^{-3}$ is about $1 \mu m$. Because the SCF extends up to $5 \mu m$, our data suggest that recombination could occur at paired extended defects identified in an earlier study.¹²

The band bending (ranging from 0.2 to 0.4 eV) is calculated from the dimensions and strength of the SCF. Because the minority carriers (electrons) are attracted toward the SCF, we infer the downward direction of the band bending for the conduction band. Because the PL emission energy was the same near the extended defect, the same band bending is present for the valence band.

The band diagram is quite similar to that of the grain boundaries in polycrystalline CdTe.²⁸ It is generally accepted that grain-boundary recombination can limit the open-circuit voltage and efficiency of II–VI solar cells.^{29,30} Our data show that recombination at other extended defects could also be important—we found that in the high-quality heterostructures ($\tau_B = 560$ ns) a single extended defect could cause recombination in an area much larger than the typical crystalline grain size in CdTe, Cu(In,Ga)Se₂, kesterite, perovskite, and other thin-film solar cells. The recent research efforts have increased the charge-carrier lifetimes in polycrystalline materials (e.g., $\tau_B = 10-100$ ns in CdTe³¹ and $\tau_B \approx 400$ ns in Cu(In,Ga)Se₂³²), and the passivation of other extended defects—not only grain boundaries—could be increasingly important for thin-film solar cells. A balance of the crystalline grain size vs. the extended defect density is carefully considered for multicrystalline silicon solar cells,³³ and thin film solar cell technologies could follow similar approach.

This work was supported by the U.S. Department of Energy under Contract No. DE-AC36-08-GO28308 with the National Renewable Energy Laboratory. The U.S. Government retains and the publisher, by accepting the article for publication, acknowledges that the U.S. Government retains a nonexclusive, paid up, irrevocable, worldwide license

to publish or reproduce the published form of this work, or allow others to do so, for the U.S. Government purposes.

- ¹J. M. Burst, J. N. Duenow, D. S. Albin, E. Colegrove, M. O. Reese, J. A. Aguiar, C.-S. Jiang, M. K. Patel, M. M. Al-Jassim, D. Kuciauskas, S. Swain, T. Ablekim, K. G. Lynn, and W. K. Metzger, *Nat. Energy* **1**, 16015 (2016).
- ²Y. Zhao, M. Boccard, S. Liu, J. Becker, X.-H. Zhao, C. M. Campbell, E. Suarez, M. B. Lassise, Z. Holman, and Y.-H. Zhang, *Nat. Energy* **1**, 16067 (2016).
- ³D. J. Wolford, G. D. Gilliland, T. F. Kuech, J. A. Bradley, and H. P. Hjalmarson, *Phys. Rev. B* **47**, 15601 (1993).
- ⁴T. H. Gfroerer, C. M. Crowley, C. M. Read, and M. W. Wanlass, *J. Appl. Phys.* **111**, 093712 (2012).
- ⁵T. H. Gfroerer, Y. Zhang, and M. W. Wanlass, *Appl. Phys. Lett.* **102**, 012114 (2013).
- ⁶F. Chen, Y. Zhang, T. H. Gfroerer, A. N. Finger, and M. W. Wanlass, *Sci. Rep.* **5**, 10542 (2015).
- ⁷B. Fluegel, K. Alberi, M. J. DiNezza, S. Liu, Y.-H. Zhang, and A. Mascarenhas, *Phys. Rev. Appl.* **2**, 034010 (2014).
- ⁸K. Alberi, B. Fluegel, M. J. DiNezza, S. Liu, Y.-H. Zhang, and A. Mascarenhas, *Appl. Phys. Express* **7**, 065503 (2014).
- ⁹D. Kuciauskas, K. Wernsing, S. A. Jensen, T. M. Barnes, T. H. Myers, and R. A. Bartels, *IEEE J. Photovoltaics* **6**, 1581 (2016).
- ¹⁰K. Alberi, B. Fluegel, H. Moutinho, R. G. Dhere, J. V. Li, and A. Mascarenhas, *Nat. Commun.* **4**, 2699 (2013).
- ¹¹W.-J. Yin, J.-H. Yang, K. Zaunbrecher, T. Gessert, T. Barnes, Y. Yan, and S.-H. Wei, *Appl. Phys. Lett.* **107**, 141607 (2015).
- ¹²K. N. Zaunbrecher, D. Kuciauskas, C. H. Swartz, P. Dippo, M. Edirisooriya, O. S. Ogedengbe, S. Sohal, B. L. Hancock, E. G. LeBlanc, P. A. R. D. Jayatilaka, T. M. Barnes, and T. H. Myers, *Appl. Phys. Lett.* **109**, 091904 (2016).
- ¹³D. Kuciauskas, A. Kanevce, J. M. Burst, J. N. Duenow, R. Dhere, D. S. Albin, D. H. Levi, and R. K. Ahrenkiel, *IEEE J. Photovoltaics* **3**, 1319 (2013).
- ¹⁴A. M. Allende Motz, J. Squier, D. Kuciauskas, S. Johnston, A. Kanevce, and D. Levi, in *Proceedings of the 42nd IEEE Photovoltaic Specialists Conference, New Orleans, LA, USA* (2015).
- ¹⁵E. S. Barnard, E. T. Hoke, S. T. Connor, J. R. Groves, T. Kuykendall, Z. Yan, E. C. Samulon, E. D. Bourret-Courchesne, S. Aloni, P. J. Schuck, C. H. Peters, and B. E. Hardin, *Sci. Rep.* **3**, 2098 (2013).
- ¹⁶D. Kuciauskas, S. Farrell, P. Dippo, J. Moseley, H. Moutinho, J. V. Li, A. M. Allende Motz, A. Kanevce, K. Zaunbrecher, T. A. Gessert, D. H. Levi, W. K. Metzger, E. Colegrove, and S. Sivananthan, *J. Appl. Phys.* **116**, 123108 (2014).
- ¹⁷A. Kanevce, D. Kuciauskas, D. H. Levi, A. M. Allende Motz, and S. W. Johnston, *J. Appl. Phys.* **118**, 045709 (2015).
- ¹⁸B. Gaury and P. M. Haney, *J. Appl. Phys.* **119**, 125105 (2016).
- ¹⁹J. D. Morris, T. L. Atallah, C. J. Lombardo, H. Park, A. Dodabalapur, and X. Y. Zhu, *Appl. Phys. Lett.* **102**, 033301 (2013).
- ²⁰T. Manaka, E. Lim, R. Tamura, and M. Iwamoto, *Nat. Photonics* **1**, 581 (2007).
- ²¹K. Wu, J. D. Canterbury, P. T. Wilson, and M. C. Downer, *Phys. Status Solidi* **3085**, 3081 (2003).
- ²²J. I. Jang, S. Park, D. J. Clark, F. O. Saouma, D. Lombardo, C. M. Harrison, and B. Shim, *J. Opt. Soc. Am. B* **30**, 2292 (2013).
- ²³Y. Cho, F. Shafiei, B. S. Mendoza, M. Lei, T. Jiang, P. S. Ho, and M. C. Downer, *Appl. Phys. Lett.* **108**, 151602 (2016).
- ²⁴C. Li, Y. Wu, T. J. Pennycook, A. R. Lupini, D. N. Leonard, W. Yin, N. Paudel, M. Al-Jassim, Y. Yan, and S. J. Pennycook, *Phys. Rev. Lett.* **111**, 096403 (2013).
- ²⁵T. Karin, "Optical and spin properties of defect-bound excitons in semiconductors," Ph.D. thesis, University of Washington, 2016.
- ²⁶T. Karin, X. Linpeng, A. K. Rai, A. Ludwig, A. D. Wieck, and K.-M. C. Fu, in *Proceedings of the 43rd IEEE Photovoltaic Specialists Conference, Portland, OR, USA* (2016).
- ²⁷Y. Yan, M. M. Al-Jassim, K. M. Jones, S.-H. Wei, and S. B. Zhang, *Appl. Phys. Lett.* **77**, 1461 (2000).
- ²⁸C. Li, Y. Wu, J. Poplawsky, T. J. Pennycook, N. Paudel, W. Yin, S. J. Haigh, M. P. Oxley, A. R. Lupini, M. Al-Jassim, S. J. Pennycook, and Y. Yan, *Phys. Rev. Lett.* **112**, 156103 (2014).
- ²⁹J. Moseley, W. K. Metzger, H. R. Moutinho, N. Paudel, H. L. Guthrey, Y. Yan, R. K. Ahrenkiel, and M. M. Al-Jassim, *J. Appl. Phys.* **118**, 025702 (2015).
- ³⁰J. Moseley, M. M. Al-Jassim, H. L. Guthrey, J. M. Burst, J. N. Duenow, R. K. Ahrenkiel, and W. K. Metzger, *J. Appl. Phys.* **120**, 105704 (2016).
- ³¹S. A. Jensen, J. M. Burst, J. N. Duenow, H. L. Guthrey, J. Moseley, H. R. Moutinho, S. W. Johnston, A. Kanevce, M. M. Al-Jassim, and W. K. Metzger, *Appl. Phys. Lett.* **108**, 263903 (2016).
- ³²S. A. Jensen, S. Glynn, A. Kanevce, P. Dippo, J. V. Li, D. H. Levi, and D. Kuciauskas, *J. Appl. Phys.* **120**, 063106 (2016).
- ³³D. B. Needleman, H. Wagner, P. P. Altermatt, Z. Xiong, P. J. Verlinden, and T. Buonassisi, *Sol. Energy Mater. Sol. Cells* **158**, 29 (2016).